ELSEVIER

Contents lists available at ScienceDirect

Ultramicroscopy

journal homepage: www.elsevier.com/locate/ultramic





Correction of artefacts associated with large area EBSD

B. Winiarski ^{a,c}, A. Gholinia ^{a,d,*}, K. Mingard ^b, M. Gee ^b, G. Thompson ^a, P.J. Withers ^{a,d}

- ^a Department of Materials, University of Manchester, Manchester, M13 9PL, United Kingdom
- ^b Materials Division, National Physical Laboratory, Teddington, TW11 0LW, United Kingdom
- ^c Thermo Fisher Scientific, 62700 Brno, Czech Republic
- d Henry Royce Institute, Department of Materials, University of Manchester, Manchester, M13 9PL, United Kingdom

ARTICLE INFO

Keywords: Serial block face sectioning electron microscopy (SBFSEM) Broad ion beam polishing electron back scatter diffraction focused ion beam (FIB) Computed tomography (CT) Cermet

ABSTRACT

There is an increasing requirement for the acquisition of large two (2D) or three (3D) dimensional electron back scattered diffraction (EBSD) maps. It is a well-known, but largely neglected fact, that EBSD maps may contain distortions. These include long-range distortions, which can be caused by the interaction of the electron beam with the sample geometry and it can also arise from sample or beam drift. In addition there are shorter range artefacts arising from topographical features, such as curtaining. The geometrical distortions can be minimised by careful SEM calibrations and sample alignment. However, the long-range distortions become increasingly prevalent when acquiring large area 2D EBSD maps which take a long time to acquire and thus are especially prone to drift. These distortions are especially evident in serial section tomography (SST) when 2D maps are stacked on top of one another to produce 3D maps. Here we quantify these distortions for large area EBSD data by referencing them to secondary electron (SE) images for 3D-EBSD data acquired on a WC-Co hardmetal. Longrange distortions (due to drift) equating to around 10μm across a 200μm x 175 μm area map, and short-range distortions (due to topographical effects) as large as 3 µm over a distance of 40 µm were observed. Methods for correcting these distortions are then proposed. This study illustrates the benefits and necessity of such corrections if morphological features are to be properly interpreted when collecting large 3D EBSD datasets, for example by mechanical sectioning, serial block face SEM ultramicrotomy, laser sectioning, FIB-SEM tomography, PFIB spin milling, etc.

Introduction

Electron back scattered diffraction (EBSD) can provide unique information about the crystallographic nature and orientation of the grains comprising polycrystalline materials. Typically, the sample is tilted for EBSD analysis, where the high sample tilting can influence the scanned area to produce image distortions in the 2D EBSD maps. The distortions can be divided into two types, namely long-range and short-range distortions. The long-range distortions can arise either from the geometrical relationship between the sample and the beam or from the sample and beam drift [1–3]. The short-range artefacts can arise from topographical features, such as curtaining [4].

Geometric distortions can appear if the sample surface is not ideally orientated with respect to the beam. For example, this can arise from an incorrect tilt angle if the sample is not correctly aligned with respect to the tilt axis. The other source of geometric large range distortion can be because of beam distortions in the scanning electron microscope (SEM)

at low magnifications [1,2,5]. The geometric distortions can be minimised to a large extent by taking care with orthogonal sample surface preparation, calibration of the secondary electron (SE) image and stage and ensuring that the area of analysis is kept within the limits of the SEM capability in order to minimise beam distortions.

Over recent years there has been an increasing trend towards the acquisition of very large area EBSD maps, aided in part by faster EBSD detector technology, refined EBSD pattern centre calibration and improvements in software for stitching together large scans extending across several millimeters [6–9]. In such cases one can decrease resolution and use fast acquisition to limit the image distortion, due to drift, to less than a pixel. However, the time required for large area and high resolution EBSD can become very long introducing drift and long-range image distortion into the 2D EBSD maps [1,10–12]. Often these distortions are neglected.

Alongside the move towards mapping larger areas there is an increasing need for highly detailed three dimensional (3D)

E-mail address: ali.gholinia@manchester.ac.uk (A. Gholinia).

^{*} Corresponding author.

B. Winiarski et al. Ultramicroscopy 226 (2021) 113315

microstructural data across a wide variety of systems [13], either to understand performance (e.g. the permeability of porous networks), or as an input to image-based numerical models [14]. 3D maps are usually obtained through destructive serial sectioning techniques [15,16]. This can be achieved using a variety of material removal methods according to the volumes to be interrogated including mechanical sectioning [17-20], microtomy [21], SEM ultra-microtomy [22,23], laser sectioning [24], plasma beam sectioning [25], broad ion beam (BIB) [11,16,26], plasma-focused ion beam (PFIB) spin milling [27] and focused ion beam (FIB) milling [28-32]. In all the above cases some form of reconstruction is required in order to bring a stack of 2D image slices into registry to form a 3D image. Post-processing and image segmentation of the data set usually only takes into account rigid body motions, i.e. X-Y alignment and rotation of individual slice images caused by the additional stage movements between milling and imaging operations [17-19,28-32]. In such cases unless corrected for, the image distortions can give a very misleading picture of grain morphologies and grain boundary relationships.

The grain size distribution of typical materials varies from submicron to tens of microns, thus statistically reliable 2D map can be several milli-meters across and a 3D reconstruction of serial sectioned volumes of materials requires large SE images and EBSD maps more than 200 µm across, which can be acquired with sub-micron resolution. SE images can typically be acquired within seconds, where sampling speeds are about $10 - 30 \,\mu s$ per point. However, even present EBSD detectors can only achieve acquisition speeds an order of magnitude slower (over 200 µs per point). Furthermore, these speeds cannot be achieved for all applications, where quality of the data can be compromised, such as in cases where there is poor pattern quality, low signal to noise and signal to background ratios, multiple phases with low symmetry, pseudosymmetry and complex crystal structures and highly deformed microstructures. This means EBSD data are often mapped at a dwell time per pixel of around one to three orders of magnitude longer than SE imaging, which for large maps results in acquisition times of hundreds of minutes per map.

As a result large area scans can be undertaken rapidly by SE imaging, where image distortions and drift can be kept to less than a pixel [10], by using a combination of suitable beam dwell time, image pixel resolution and high enough magnification to minimise lens distortions, where applications can be found in digital image correlation (DIC) techniques [33-36]. However, acquiring an EBSD map can be much slower, therefore the electron beam or the sample are prone to drifts away from the assumed position leading to long-range image distortions during the acquisition of an EBSD map [1,37,38]. Furthermore, SE images are usually taken at 0° stage tilt or incidence angle, while EBSD maps are taken at 70° stage tilt or incidence angle. Therefore, the EBSD maps have 1/cosine(70°) or 2.9 times smaller beam spacing or deflection in the direction perpendicular to the tilt axis in order to generate an equidistant grid of measurements points on the sample surface. This results in almost a threefold degradation in spatial resolution and increase of any effect from drift or 'long-range distortion', furthermore it accentuates the distortion from topographic features or 'short-range distortion', in the EBSD maps [12]. Thus, these distortion exaggerations are minimised during SE imaging at 0° incidence angle. This is also one of the advantages of the relatively new technique of transmission EBSD (t-EBSD) or transmission Kikuchi diffraction (TKD), where the sample is usually back tilted only between 0°-20° [39-42]. New approaches to EBSD analysis, such as the 'Dictionary based indexing' [43,44] or smart acquisition [45] promise faster acquisition times without compromising EBSD indexing rates, because either lower quality EBSD patterns and faster EBSD mapping speeds can be used or already utilizes other SEM imaging modes taken at higher speeds and requires less sampling points. Nevertheless, EBSD analysis will continue to be much slower than conventional image acquisition and thus more susceptible to drifts.

In a previous paper, we introduced serial section broad ion beam tomography and identified distortions in large area 2D EBSD maps [11].

It was shown that these can seriously affect the interpretation of 3D EBSD datasets if uncorrected through an exemplar study of the 3D microstructure of WC-Co hard metals. In this follow-up paper we return to this problem to examine the nature and to quantify the magnitude of the long-range and short-range distortions associated with acquiring large area 2D EBSD data. All imaging modes in the SEM can have distortions, however to correct for the large distortions encountered in the EBSD maps we assume that SE images are distortion free compared to the EBSD maps. Furthermore, we propose methods for correcting both of long and short-range distortions by comparing EBSD maps to SE images. Our proposed methods utilise COSFIRE, Combination of Shifted Filter Responses filters [46] and Moving Least Squares (MLS) rigid deformation method for digital image morphing [47]. The aim of this paper is to raise awareness of these artefacts which are largely neglected at present, to quantify them and to show the benefits of their correction. This paper is not aimed at proposing the best method of correction, nor comparing the merits of specific correction approaches, but rather to encourage a greater focus on developing such methods going forwards.

By way of a case study, this paper focuses on distortions associated with collecting relatively large volume serial section data on WC-Co hard metals (or cermets). They are used for machining, cutting, mining and drilling and are challenging because they contain a high fraction of a ceramic phase (i.e. the WC grains) held together by a ductile metallic phase (i.e. the Co). The mechanical properties of cemented carbides strongly depend on the size and morphology of the WC grains [48,49]. Abnormal grain growth (AGG) can have a detrimental effect on the mechanical properties of cermets, since these oversized grains (typically > 10 - 30 µm) act as nucleation points for cracking, breakage and drill bit failure. The mechanism for AGG is not yet sufficiently understood. Some attempts have been made to simulate AGG in cemented carbide verified with experimental work and 2D analyses [50], but the plethora of information that can be extracted from 3D analyses allows the opportunity to much more fully study the AGG phenomenon. It must be noted here that there are non-destructive techniques available to study AGG during in-situ heating [51,52], however the resolution of these techniques are presently about 1 µm. Although FIB-SEM based techniques are destructive, but are able to resolve volumes in 3D in nanometre resolution. Large area plasma FIB [25], BIB-SEM [16], laser-PFIB-SEM [24] or PFIB spin milling methods [27] are needed to capture data over microstructurally relevant large volumes. As a result, such EBSD data provides a good case for quantification and correction of long and short-range corrections described in this paper.

Experimental procedure and SE-EBSD image pair co-registration

As mentioned above, the focus of the current paper is on the quantification of long and short-range distortions associated with large area EBSD mapping and methods for their correction rather than on making serial sectioning experiments per se. To this end we return to the 3D EBSD dataset collected by serial section BIB for the WC—Co hardmetal sample described in [11].

Sample

The material studied was a Tungsten carbide and Cobalt (WC—Co) hardmetal containing 11 mass% Co and having the average grain diameter of 5 μ m [53]. The alloy was produced by Marshalls Hard Metals Ltd using conventional powder metallurgical methods. Tungsten carbide (WC) has a hexagonal crystal structure with lattice parameters a=2.9 Å and c=2.83 Å. The stable Cobalt (Co) phase has a cubic crystal structure with a lattice parameter size a=3.56 Å.

Broad ion beam sectioning

The experimental BIB serial sectioning workflow followed in this

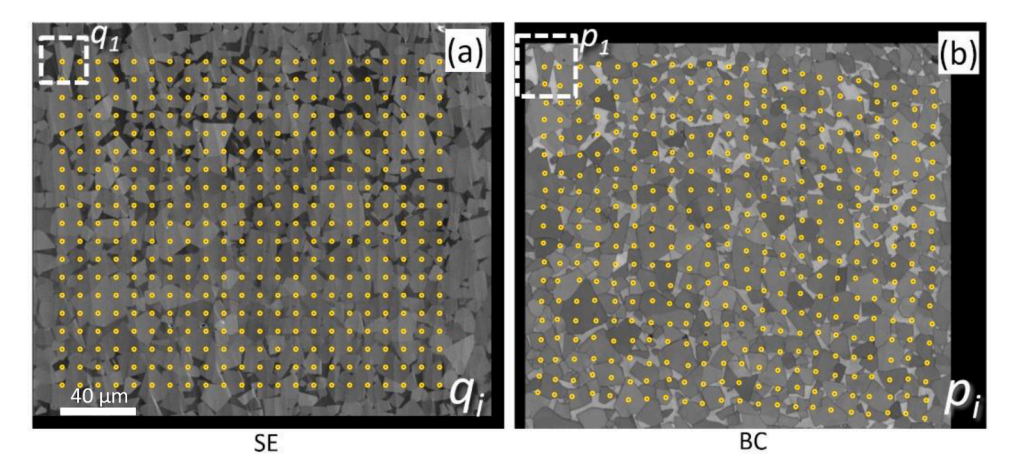


Fig. 1. Long-range co-registration, COSFIRE only. (a) shows the grid of points, q_b generated on the reference SE image; (b) shows the corresponding grid of points, p_b located on the BC image clearly showing the distortion. The dashed squares mark the search vicinity for points q_1 and p_1 .

study is described in detail in a companion paper [11]. In essence, the sample was manually passed between a Gatan, Ilion broad ion beam system and a dual beam FEI NOVA600i FIB-SEM. The milling conditions were 5 kV, 60 μA with 20 min mill time per slice, where the average slice thickness was 700 nm. After each material removal step a secondary electron (SE) image of the surface was collected using the SEM at 0° sample tilt, after which the crystallographic information was collected by EBSD mapping at 70° sample tilt, to form SE-EBSD image pairs. The quality of Ar^+ ion polish achieved by with the Ilion BIB results in a very good surface for EBSD analysis without significant damage or phase transformation facilitating high indexing rates (above 90%). The co-registration of successive images was achieved using markers made by FIB [11].

SE-EBSD image pairs

Presently, it is possible to undertake EBSD analysis for areas of several mm² dimensions by combining scanning of a large area by moving the electron beam and the stitching multiple scanned areas using the stage [6-8]. Although the size of the maps analysed here are relatively modest compared to the largest ones reported elsewhere the distortion corrections applied here are applicable to much larger areas too. The EBSD maps used in this work were acquired at 200 nm step size with map size of $205 \times 177 \, \mu m$ ($1024 \times 884 \, pixels$) and were taken at 70° angle of incidence and sample tilt using a Nordlys-S EBSD detector from Oxford Instruments plc. This EBSD map size is relatively large for an ion based serial section tomography (SST) technique. The EBSD settings were chosen for the purpose of 3D-EBSD analysis. Therefore, to ensure an accurate and high indexing percentage and to minimise mis-indexing for the WC and Co phases, a relatively high resolution EBSD detector setting of 4 \times 4 binning (336 \times 256 pixels) was used, which means that the indexing time was about 25 ms per point, equivalent to 40 Hz, giving about 6 h acquisition time per slice. Therefore the EBSD settings used here resulted in an unusually slow speed for gathering an EBSD map per slice, however this meant that the average indexing rate was very high (> 96%) [11] and the risk of low quality EBSD data was minimised for every slice. Furthermore, the slow EBSD mapping speed exaggerated any possible distortion effects from drift. Note that the Nordlys-S EBSD detector has a CCD technology camera and is a slower detector compared to the newer EBSD detectors based on CMOS technology cameras. The crystallographic orientation at each point on every section was determined by Channel 5 software [54], creating band contrast (BC) and inverse pole figure (IPF) coloured orientation maps showing the crystallographic orientations of the grains. The BC maps, which have distinctive microstructural features, were used for the SE-EBSD image pair co-registration, see Fig. 1b.

For this work the EBSD maps were acquired first, however this is not usually done for routine EBSD analysis. This was done to minimise any possible contamination or interference from secondary electron (SE) imaging that may otherwise compromise the quality of the EBSD patterns. Subsequently, SE images were acquired at 0° angle of incidence at the same pixel (0.2 $\mu m \times 0.2~\mu m$) and image (1024 \times 884 pixels) size as the EBSD maps after the acquisition of the EBSD maps, see Fig. 1a. This order of analysis also helped to easily locate the contaminated region left from the EBSD analysis to ensure the same region was chosen for SE imaging and minimise any drift errors.

The long-range distortion correction procedure

The SE-EBSD image pairs are co-registered using the so-called 'Long-Range Co-registration' (LRC) approach to quantify the long-range distortions. Our automated co-registration algorithms embedded in standalone Matlab-based software uses trainable COSFIRE contour-based pattern recognition algorithms [46] to detect arrays of points for characteristic microstructural features in the SE-EBSD image pair sets. In this way a reference square grid generated on a SE image are mapped to a deformed grid located on the associated EBSD map, by an automatic trainable algorithms and then uses the Moving Least Squares (MLS) rigid deformation method for digital image morphing [47]. The co-registration process uses the SE and BC images pairs to correct for long-range distortions. The corrections are then applied to all other the EBSD maps. Therefore, not only the BC images but also the IPF colour orientation and EBSD phase maps are simultaneously corrected.

Firstly, the LRC software, automatically generates a square array of points having a pixel spacing, q_i , as the reference and non-distorted array on the SE images, as seen as the small white dashed square in Fig. 1a. An initial pixel spacing, q_i , is chosen to be on the order of the average grain diameter. Here, where the average grain diameter is 5 μ m, a 40 pixel spacing (8 μ m distance spacing) was chosen, shown with the array of 22 \times 19 points in Fig. 1a.

Secondly, to map the distortion, the COSFIRE-based microstructure recognition algorithms automatically locates the corresponding points, p_i , (as the distorted array of points on the BC images) across a square search area of 100×100 pixels, as seen as the small white dashed square in Fig. 1b. Details of the COSFIRE filter [46] are described in the appendix, entitled 'COSFIRE filters for microstructure pattern recognition'. In case, the algorithm misinterprets any of the features on the BC image, the user can manually locate the corresponding points, p_i , and train the algorithm. This is a pre-deep learning method, where these initial attempts are semi-automatic by manually looking at overlay of the image pairs for features existing in both images, such as boundaries. It is clear that the long-range distortion of the EBSD image is significant,

B. Winiarski et al. Ultramicroscopy 226 (2021) 113315

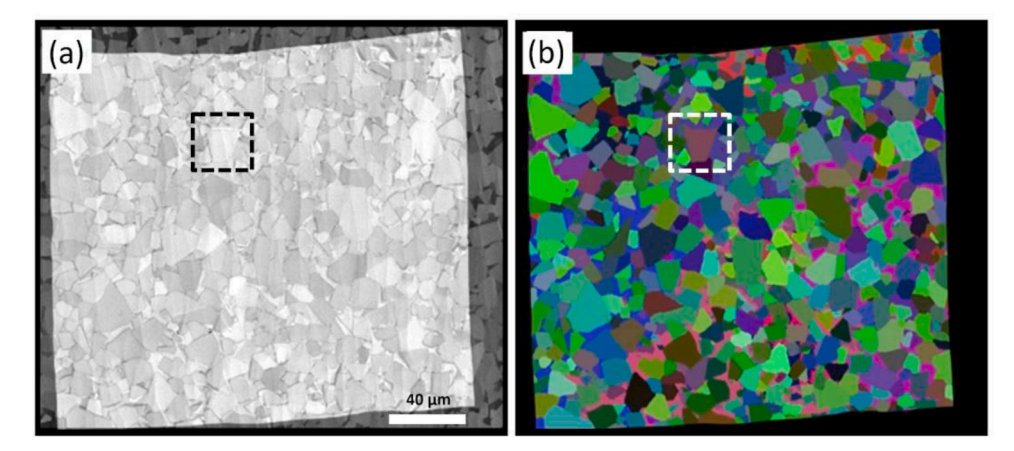


Fig. 2. 'Long-Range Co-registration' using COSFIRE and MLS moving least squares image morphing: (a) shows the co-registered (corrected) BC image superimposed on the SE reference image; (b) the corresponding EBSD map in random colours generated by AVIZO. Dashed rectangles mark areas co-registered using the short-range co-registration (see details in the next section, entitled 'The short range distortion correction procedure').

which is around (-13, 52) pixels in the bottom right-hand corner, equivalent to an error of (-2.6, 10.7) microns. The larger distortion values in y-direction are influenced by the high sample tilt during EBSD analysis [1,12].

Thirdly, in order to correct the distortion, the BC and IPF image stacks are deformed using the Moving Least Squares rigid morphing method (find a concise description in the appendix, entitled 'Moving Least Squares for digital image deformation' or more details in [47]). Fig. 2a shows an example of a BC image from the stack superimposed on the SE reference image, which is co-registered and LRC corrected. Fig. 2b shows the corresponding EBSD grain map.

Fourthly, a verification test is run to optimise the q_i spacing to find the least number of points and give a good balance between the quality of co-registered image pairs and computational effort and time for co-registration. This is done iteratively, in only a small part of the map to reduce computation time, until the overlay is optimised. Here the final chosen pixel spacing was kept the same as the initial 40 pixels spacing, because it was found to be an acceptable compromise between quality and computation time.

Finally, the optimised LRC co-registration correction is run for the whole volume image stack and the co-registered IPF image stack is fed directly to the 3-D analysis software, where the grains are segmented for visualisation and quantitative analyses (see details in the next section, entitled 'The short range distortion correction procedure').

Here we should note that the above mentioned correction assumes that the slice thicknesses are constant and does not correct for any varying slice thickness, as has been shown to be important in our earlier publication [11]. Therefore, in the images in Figs. 1 and 2 there may be errors caused by thickness variations across the sample, which may partly influence the variation in the angle of distortion correction seen

across the map in Fig. 2, but they are not considered here. To correct for this an accurate surface profile measurement of each slice is needed and is beyond the scope of this paper and is planned for future work. However local variations caused by milling, such as curtaining will be discussed in the next section.

Furthermore, note that the WC is seen as the lighter grey phase compared to the Co phase in the SE images, whereas the reverse contrast can be seen in the BC maps, thus the Co phase is seen as the brighter phase. SE images contain mainly secondary electron and some back-scatter electron signals, therefore the contrast is influenced primarily by topography and to some extend by orientation and backscattered electron intensity that is influenced by atomic number. The average atomic number in the WC phase is higher than the Co phase, therefore it has a higher contrast in the SE images.

The band contrast (BC) values are the average intensity of the detected bands in each phase, which not only contain orientation contrast, backscattered electron intensity but also intensity from the detected Kikuchi bands and EBSD pattern quality [55]. The reversal of contrast between the phases in the BC image can be because of the probability of higher intensity bands detected in the Co phase than in the WC phase. The Co phase has a cubic crystal structure with higher symmetry and the main bands have higher intensity compared to other bands, whereas in the WC phase there is less difference in band intensities, as seen in the EBSD patterns in Fig. 3. Furthermore, the Co phase is softer and easier to polish with BIB milling, but WC phase is susceptible to ion beam damage which can result in poorer EBSD patterns from the WC phase compared to the Co phase [25].

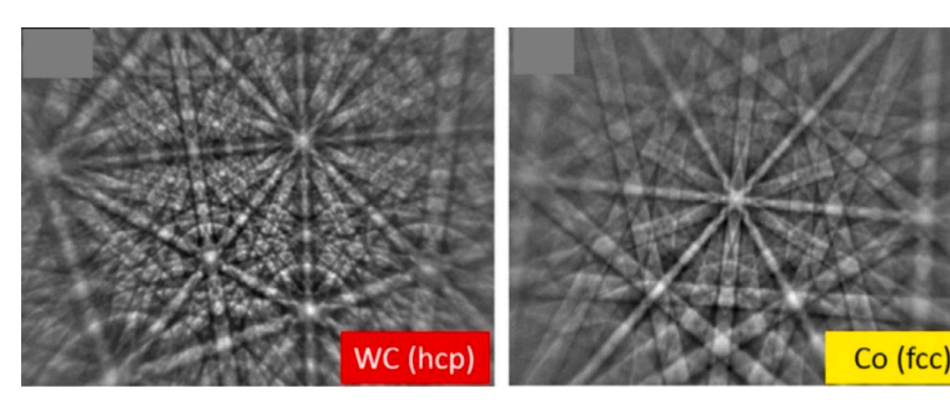
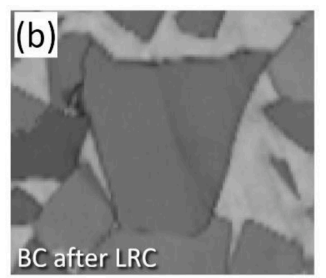


Fig. 3. Example EBSD patterns from WC and Co phases [25].



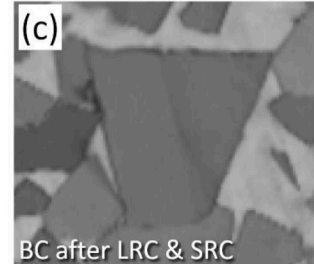


Fig. 4. Long-Range Co-registration (LRC) and Short-Range Co-registration (SRC) are applied: (a) the reference SE image; (b) BC image obtained from LRC; (c) BC image after LRC+SRC corrections. Images are 40 μm across.

The short-range distortion correction procedure

Curtaining/polishing effects are a common problem for serial sectioning [15,26,56]. As a result surface topographies can vary significantly (in our case by up to ± 300 nm [11]) from a perfectly flat surface and vary significantly from slice to slice. EBSD mapping of such surfaces can incur a distinctive local image distortion, see Figs. 4a and 4b. To quantify and correct such short-range artefacts our software can apply a 'Short-Range Co-registration' (SRC), as shown in Fig. 4c. Presently, this step requires manual selection of points to define corresponding features in both SE and BC images. The software calculates 2D displacement fields from the difference of spatial positioning between the selected points in the SE and BC images. An automatic MLS image morphing algorithm uses the points to correct the BC images. More details of this process are provided in the appendix, entitled 'Short-range co-registration description'.

This procedure is repeated for all the images from the stack and the corrected BC and IPF image stacks are read into the FEI AVIZO software.

We note that this method can correct distortions in pixel resolution when SE images are used as reference. However, we should remind the reader of the assumption here is that the SE images are 'free of distortion'. Therefore, it is difficult to measure the true errors of the corrections in 2D without a completely distortion free reference. However, the errors relating to the correction will be discussed in 3D, in the results and discussion section.

In the WC—Co system used as an example here, there is a high atomic number contrast between the two WC and Co phases, which makes it easy to locate common features between the SE and BC images. Similarly, other features maybe used, such as grain boundaries, second phase particles, cracks, deformation bands and other distinguishable features that may be recognisable between the two SE and BC images. Consequently, this correction method is only possible in the presence of distinguishing features.

3D EBSD data visualization

Once corrected by the co-registration of the SE-EBSD image pairs, the IPF image stacks are transferred to 3D visualisation and analysis software (FEI AVIZO Standard/Fire). Here, the images are aligned using a least-squares minimisation method [57]. The layers are spaced using the average slice thickness of the measured stacks (see Section 3.3 in [11]) at 700 nm. The individual grains are segmented within the images. The segmentation process using the colour (RGB) values for thresholding is straightforward, since each orientation has a different colour and the grain boundaries are well defined.

It must be noted that, in this work the corrected 3D data are visualised using EBSD images displayed in IPF colours. This is sufficient orientation information, with IPF colours, to study the shape and facets of individual grains. However, the full crystallographic information required for the pole figures are taken from each of the individual 2D EBSD maps. In this paper, this type of information and visualisation software was sufficient to highlight and study the distortion corrections.

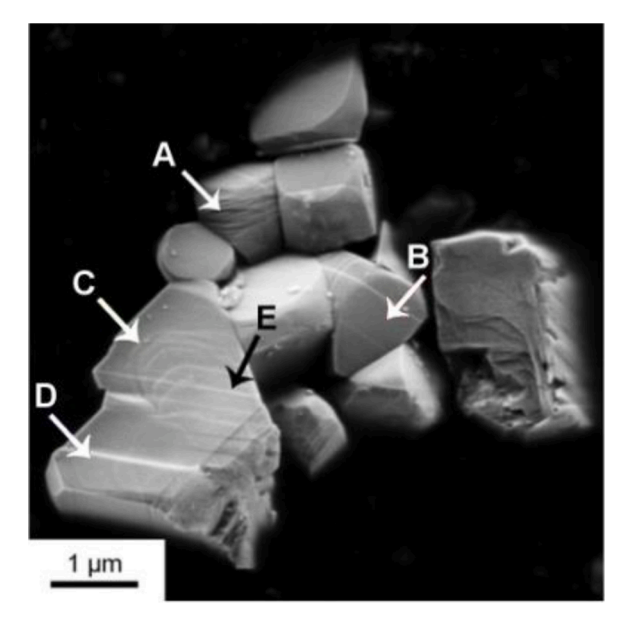


Fig. 5. Grains extracted from the Co matrix for WC-20%wt. Co alloy [32]. The A arrow marks a non-faceted grain surface, the B arrow shows a faceted grain surface, the C arrow points stepped (terraced) surface structure, the D arrow shows a terrace step, and the E arrow shows a stepped defect.

However, the corrections maybe be applied to other types of 3D EBSD visualisation software too.

Results and discussion

The hard WC grains lie within a matrix of ductile Co matrix fabricated by liquid-phase sintering. During sintering the average carbide grain size increases by means of grain coarsening as large grains grow and small grains dissolve by an Ostwald ripening mechanism. The majority of the large WC grains have a faceted shape and have a strong tendency for clustering, and abnormal grain growth [32,50,58–61]. The facets can be dozens of nanometres in size and equiaxed [32]. In this study, the facets are used as a measure to analyse the quality of the reconstruction after distortion corrections.

Both faceted and non-faceted surfaces with terrace-like faces may be present in WC grains, where the larger grains are reported to be the result of abnormal grain growth (AGG) that are a consequence of grains containing step defects [32,61], see Fig. 5. However, in this study the large grains are assumed to have planar facets and the steps are neglected, because the steps are usually smaller, only a few nanometers, than the resolution of the voxels size, $200 \times 200 \times 700$ nm, in the dataset used here.

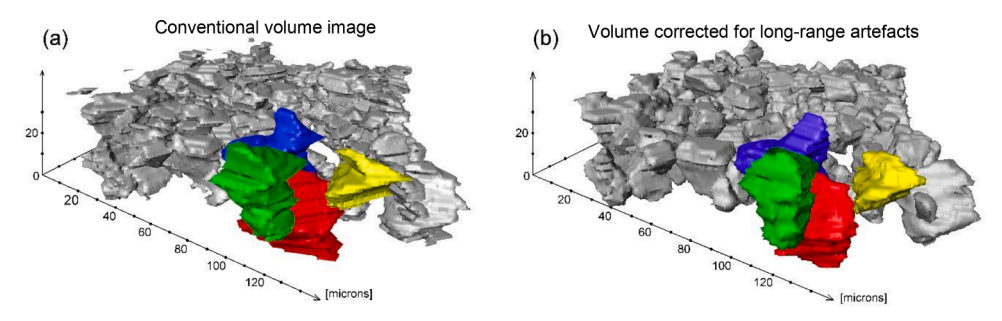


Fig. 6. 3D reconstruction of the microstructure of WC grains in WC-11 wt.% Co cermet sectioned by Ilion broad ion beam a) prior to and b) after correcting only the long-range distortion artefacts. Note: a random colouring is applied by the Avizo visualisation software.

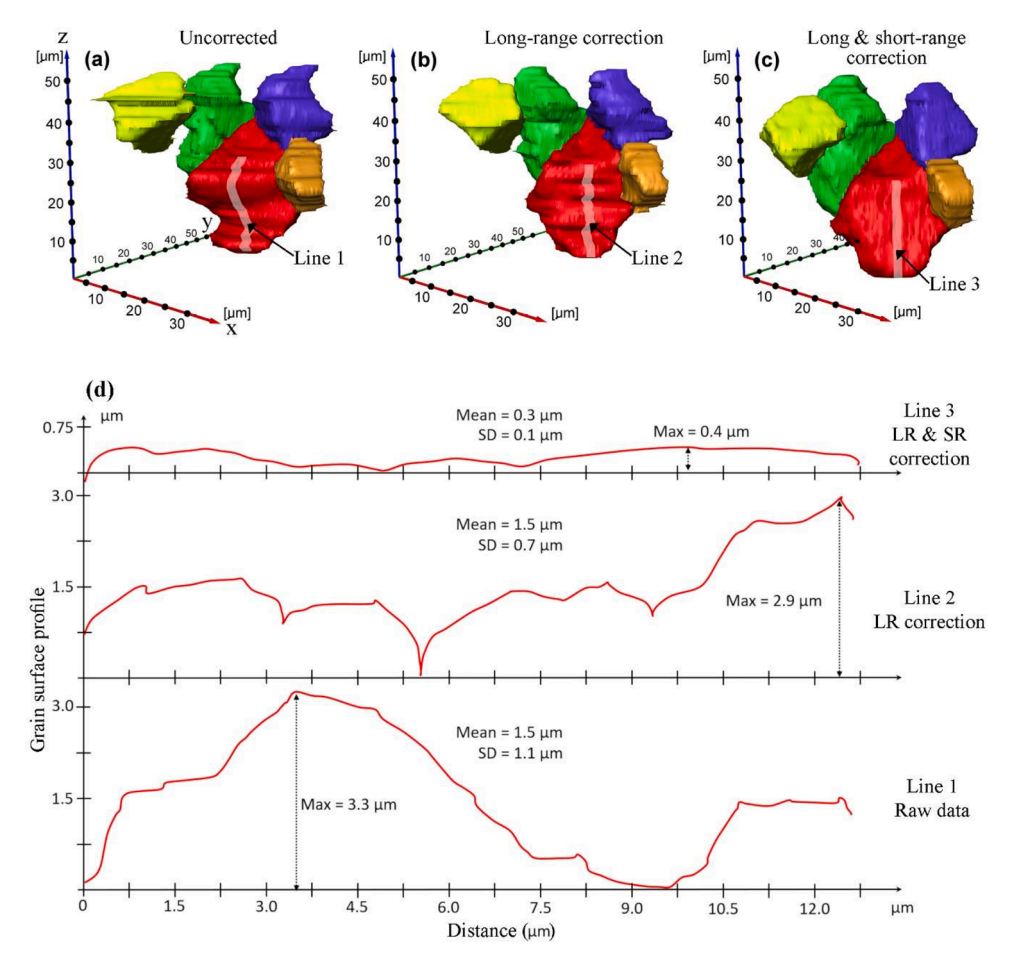


Fig. 7. Cluster of WC grains after reconstruction from EBSD image stack for different data correction schemes [16]. Lines indicate facet regions where the angular misorientation is measured from 51 measurement locations along these lines. (a) shows raw data; (b) shows results of long-range corrections; (c) shows results of long-range and short-range corrections; (d) shows measurements of grain surface line profiles.

3D analysis with long-range correction

3D analysis allows for a comprehensive quantification of key microstructural features relating to individual grains or clusters of grains, many of which cannot be recovered from a 2D section, for example the morphology of voids, grain edges, corners, grain boundary planes, triple junctions, relative energies of grain boundary facets, the effects of impingement on grain coarsening, grain voids, networks of intergranular and transgranular cracks, etc. [14,19,62,63]. In order to achieve this type of analysis it is required that the 3D data represents the real microstructure accurately. Therefore, it is necessary for any long-range and short-range distortions and artefacts to be corrected. These distortions and artefact are usually neglected, which affect the 3D

images and thus the 3D grain boundary facets, morphology and their relationship to crystallographic characterization.

The 2D-EBSD sections, for example those in Fig. 4, show evidence of the faceting of the WC grains in common with the 3D SE images of recovered WC grains in Fig. 5. However, it is evident from Fig. 6a that the uncorrected raw 3D image stacks show the reconstructed grains to be irregular. A visual inspection of the 3D reconstruction, after the correction of the long-range distortions, can be seen, with some of the more significant edge artefacts to have been corrected, as shown in Fig. 6b. However, the grains still exhibit significant artefacts, in terms of their morphologies. This may be because the long-range corrections use a grid with dimensions similar to the grain size, therefore it can be expected that the grain shape and facets would not be affected significantly

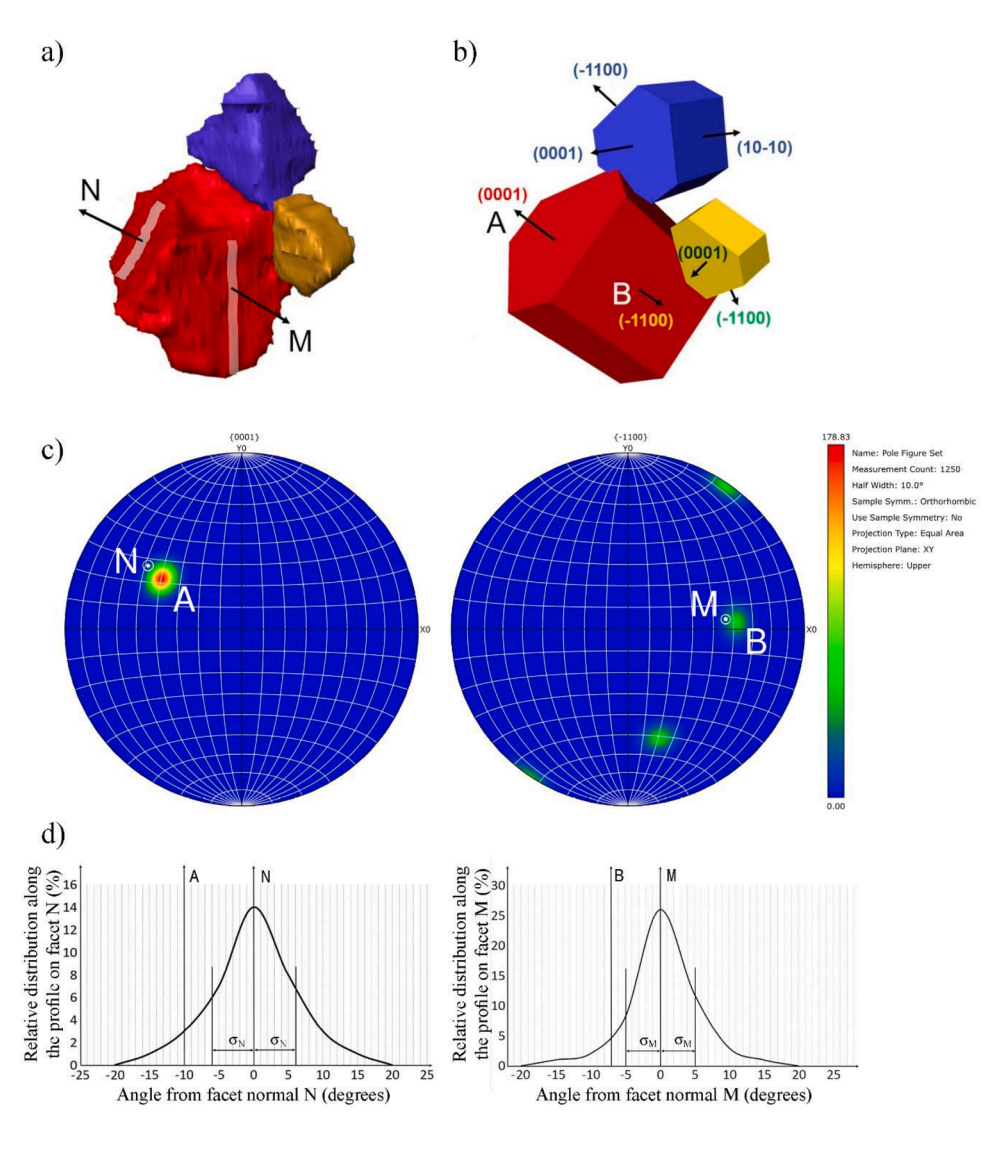


Fig. 8. Cluster of WC grains after reconstruction from EBSD image stack, showing grain facets, after both long-range and short-range data corrections. (a) shows the reconstructed grains cluster with facet normal M and N (with line profiles); (b) shows a truncated prisms model of the grains cluster based on their crystallographic orientations (the poles A and B are shown for the red WC grain); (c) pole figures for the large red WC grain and the corresponding poles of A and B, (d) relative distribution of angles from facet normal M and N along the line profiles seen in Fig. 8a and their standard deviations.

and artefact and distortions will remain at the grain level, as seen in Fig. 6b. A more detailed analysis of the grain facet roughness is discussed in the next section.

3D analysis with long and short-range corrections

Fig. 7 shows the highlighted grains in more detail, where the voxel size is 0.2 μ m x 0.2 μ m x 0.7 μ m. The line profiles 1, 2 and 3 show the extent of distortions, after each stage of distortion correction, on a grain facet, that is assumed to be planar, similar to the faceted grain surface B, shown in Fig. 5. The profiles are 2D sections across the grain facet, where the 2D section is normal to the grain facet. The distances are measured relative to the other points in the 2D section plane. The extent of LRC and SRC for distortion correction can be seen from slice to slice by the comparison of the line profiles from the raw data to the profiles after each correction step. Generally the LRC reduces the largest distortions in the raw data (here by up to 16 µm, which is twice the LRC grid spacing q_i), nevertheless significant distortions remain. However, after the SRC the distortions are minimised to below $1\mu m$. In Fig. 7, the maximum distortion in the raw data is 3.2 μm (mean 1.5 μm), after the long-range correction this reduced to 2.9 μm (mean 1.5 μm) and after the shortrange correction this was 0.4 μm (mean 0.3 μm), which is only twice the smallest dimension of a voxel with $0.2\mu m$ in x and y. Therefore, individual grains or sets of grains were further refined using short-range SE-EBSD data corrections. Fig. 7c shows cluster of grains visualized after the short-range (topographical effects) corrections. Here the edges, corners and triple junctions and especially the faces are much better recovered with respect to the reasonable assumption that the aligned feature is a faceted grain surface.

Grain facet analysis and abnormal grain growth

In Fig. 8 the large WC grains, that are more than $20\mu m$ across and are bonded by Co matrix, usually have planar facets, which resemble the shape sometimes described as, 'a prism with a truncated triangle base' [64] and are seen in Fig. 5. These planar facets, or crystal habits [65], have traces of the prismatic $\{10-10\}$ and $\{-1100\}$ and basal or basal pinacoid $\{0001\}$ planes [64]. The growth rates and sizes of the planar facets depend on the relative interface energies of the prismatic and basal planes of the WC grains and the WC—Co interface energies, which are influenced by the composition of the alloy. These anisotropic interface energies result in a faceted equilibrium WC grain shape, whereas isotropic interface energies would lead to a spherical equilibrium grain shape [61,64,66].

Consequently, from the characteristic planar facets of the WC grains the crystallographic orientation of facets can be directly defined, by comparing the normal of the facets to the crystallographic orientation of the grains. The crystallographic orientation of the grains are depicted in the truncated prism models and pole figures, such as seen in pole A that corresponds to $\{0001\}$ and pole B is $\{-1100\}$, as seen in Figs. 8b and 8c.

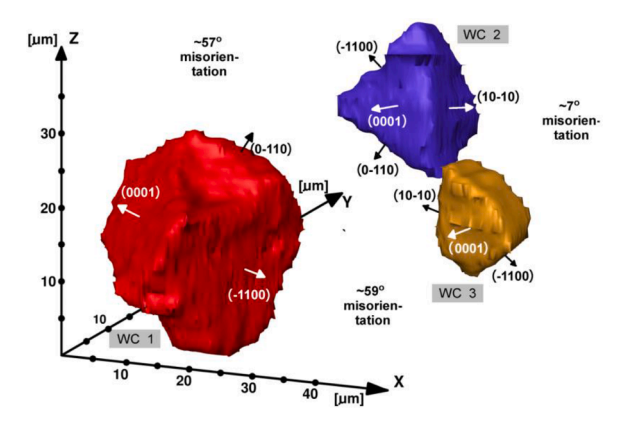


Fig. 9. Crystallographic orientations or poles are shown on the grain facets, after both the long- and short-range corrections. The misorientation angles are measured from the crystallographic EBSD data.

Therefore, by taking into account crystallographic orientations from EBSD maps, the crystallographic orientations of particular facets were defined for large well-defined WC grains and compared to their normal to the facets. The pole figures in Fig. 8c show the crystallographic poles (A and B) and their corresponding normal to the facet surfaces (N and M) with the statistical spread of standard deviation. The statistical spread from each normal M and N, along the line profiles on the facets shown in Fig. 8a, are shown in the graphs in Fig. 8d with their standard deviations of $\sigma_M=5^\circ$ and $\sigma_N=6^\circ$. Note that the line profile on facet M relates to the line profiles shown in Fig. 7. The positioning error between the crystallographic poles (A and B) and the facet normals (M and N) was reduced after LRC to $10^\circ-20^\circ$ and this was further reduced after SRC down to $7^\circ-12^\circ$ positioning error, as seen in Fig. 8d.

The smaller WC grains ($<15\mu m$ across) are not shown here, but appear more complex in shape. Very small grains ($<2~\mu m$ across) are hard to study since the voxel size of $200\times200\times700$ nm is too large to resolve them clearly. Clearly some distortions may originate from both the large voxel size and the assumption that stacked layers are parallel and of the same spacing during the 3D reconstruction for visualisation. However the different grain shapes, in the small grains, indicate that grains do not resemble the grain shapes with planar facets, similar to findings reported elsewhere [11,64]. The complex shapes of the small WC grains may suggest the possibility of grain coalescence or agglomeration of several small grains.

In contrast, the relatively large grains in Fig. 9 can be seen to have a typical faceted grain shape. Two of the WC grains have a very small contact area to each other and have a crystallographic misorientation of about 7° , which is measured from the EBSD data. Furthermore, they are constrained by a large WC grain with a high crystallographic misorientation angle from either of the two smaller grains (57° and 59°). This type of information may also help to explain the reason for abnormal grain growth of some of the grains, that are often seen in these materials, because grain growth not only depends on diffusion but also grain boundary mobility.

During sintering the average grain size increases due to coarsening or Ostwald ripening, as large grains grow and small grains dissolve [58,60,67]. However, WC grains have a strong tendency for abnormal grain growth, where the coarsening mechanism for abnormal grain growth has been reported to be driven by 2D nucleation on facets [61]. The planar facets of such large grains may have staircase like areas, that can often be observed on WC grains extracted from Co matrix in Fig. 5. However, these are difficult to be seen on the reconstructed volumes from 3D-EBSD data here, because the voxel size is too large, but we have shown this elsewhere in a smaller dataset with smaller voxel size [32].

Conclusions

Here we have examined and quantified the in-plane distortions associated with large area EBSD mapping. These comprise both longrange distortions and short-range distortions. The long-range distortions can have a variety of causes, such as drift associated with the long acquisition times, scan distortions or long-range sample alignment or surface topography. The short-range distortions maybe a consequence of local surface topography, such as 'curtaining' typically seen during ion beam milling. In practice, when large area 2D data is collected, the former artefacts are commonly ignored, while for the small area analysis the latter can be minimised by effective polishing procedures. Nevertheless, the trend towards acquiring increasingly large area 2D EBSD maps of heterogeneous across materials science and geology means that a consideration of these artefacts deserves more serious consideration going forwards. Critically, when collecting 3D serial section tomograms, the long-range drifts can seriously affect the overlay of the individual slices to form image volumes. Alongside this many serial section methods introduce topographic artefacts which give rise to short-range distortions too.

Here we have characterised both long-range and short-range artefacts for serial section tomography by BIB milling and EBSD analysis of each section of WC-11%wt.Co hard metal data collected previously [11]. We present a new methodology for SE-EBSD image pair co-registration based on trainable Combination of Shifted Filter Responses filters and two-dimensional Moving Least Squares method. Our approach and it's validation relies on three assumptions, 1) Each of our slices are planar, 2) SE images taken on the SEM, at 0° stage tilt, are distortion free and 3) the approach validation was done on the reasonable expectation of the large WC grains to have planar facets, which are reported elsewhere for similar CW-Co systems [32,50,58-61] and are also seen in etched samples [32] and the abundance of WC grains with straight grain edges or boundaries in the 2D images and EBSD analysis of polished surfaces. The alignment of the corrected facets with the expected crystallographic planes was further validation of the corrected 3D-EBSD data. This allowed 3D-EBSD data to be corrected and used for quantitative analyses and 3D visualisation. This is applied to our hard metal case study giving rise to the following conclusions:

- \bullet The cumulative long-range distortions, in the EBSD maps compared to the reference SE images, were quantified as being of the order of up to $10~\mu m$ across a $200~\times~200~\mu m$ area section. They were found to significantly affect the shapes of individual grains in 2D leading to significant errors in grain morphologies in 3D. We should note that the distortion corrections effect the shape of the grains and not the orientation.
- Curtaining effects were observed on the serial sections and the topography was measured using confocal microscopy and reported in our earlier paper [11], but the confocal microscopy measurements were not used in the correction methods here and is a subject of future work. The inclined angle of incidence leads to significant distortions (a few pixels, up to 0.3 µm) [11] of EBSD maps, given that the grains are of the order of the grid used for long-range correction, these distortions required short-range correction. Here an attempt has been made to correct the distortions in a 3D-EBSD dataset of a hard metal case, with respect to the SE images and the expectation of the 3D shapes of the hard metal grains from the chemical extracted method as discussed earlier in section 3.
- 3D visualisation clearly showed that the volume of reconstructed microstructure using the raw data was severely deformed, where surface topography for a flat facet can be as high as 3.3 μm.
- Using only the long-range correction, the topography for a planar facet, of a large well-defined WC grain, was reduced to 2.9 μm and the normal of the planar facet lay within about $10^{\circ}-20^{\circ}$ crystallographic positioning error.

• By applying the short-range corrections, the distortion corrections reduced the maximum roughness of the planar facet surface topography to 0.4 μm and the misalignment of the surface of the grain facets to their respective crystallographic planes were reduced to about 7° – 12°

These types of distortion correction algorithms are required to improve the accuracy of the EBSD maps. In this study the accuracy was based on the roughness of the reconstructed grain facets, where a suitable material was chosen that the large WC grains are known to have planar facets. Going forwards more automated procedures need to be developed so that large area EBSD maps can be routinely corrected and a more robust measure of accuracy needs to be developed. This is especially important when reconstructing 3D data because registry from layer to layer is important if features are not to be introduced into the reconstructed grain morphologies. The correction methods outlined could be applied for 2D EBSD maps and 3D EBSD maps collected at different length-scales using other SST methods, e.g. mechanical sectioning, SEM microtome, FIB-SEM tomography and the more recently developed techniques developed for large area milling such as BIB, plasma and laser technologies [15,16,68]. Furthermore, smart sampling techniques may be used for measuring accurate 3D shapes with only the imaging data and reduce the time required for orientation data measurement.

While the methods described above quantify and correct for in plane distortion, work also needs to be done to correct for the errors caused by uneven slice thickness during 3D reconstruction for visualisation to account for the actual spacing and misalignment of the successive layers in 3D-EBSD stacks. This effect has previously been shown to be significant [11]. However, use of the topography information gathered by confocal microscopy for correction is not trivial and requires further work to incorporate the topography measurements into the 3D visualisation software. This requires the software to be able to handle non-orthogonal layers, which is not the case at the moment and is the subject of future work.

Declaration of Competing Interest

The authors declare that they have no known competing financial interests or personal relationships that could have appeared to influence the work reported in this paper.

Acknowledgements

This work was supported by the grant from the University of Manchester – EPSRC – NPL research program: 3D Assessment of Surface Integrity and Performance (EP/H020047/1). Authors acknowledge GATAN for lending the prototype Illion broad ion beam system. The facilities now lie within, and are maintained through, the Henry Royce Institute through EPSRC grants EP/R00661X/1, EP/S019367/1, EP/

P025021/1 and EP/P025498/1. PJW is grateful to the ERC for advanced grant funding through CORREL-CT Grant No. 695638.

Appendices

Appendix. COSFIRE filters for microstructure pattern recognition

Combination of Shifted Filter Responses (COSFIRE) filters are able to locate 'keypoints and patterns' [46,69]. Here the filters are trained to detect keypoints, such as local microstructural features defined by the geometrical arrangements of grain boundaries, curtaining effects and surface topography. The detection filters use a range of Gabor filters [70-73], which are two dimensional characterisation of signals or information. They are usually frequency and time, but here they are frequency and orientation contrast. In order to use the correct Gabor filters the variables are adjusted, which include the amount of blurring, optimised vector shifts and the multiplier of shifted responses. First, linear Gabor filters are used for edge detection, then Gaussian blurring is applied to the Gabor responses to allow some tolerance in the position of the features, then the blurred responses are shifted by specific vectors to bring the features to the centre of the filter and multiplied for weighting. The structures of COSFIRE filters form 'fingerprints' depending on the geometric arrangement of local microstructural features, which are used to automatically train or optimise the Gabor filters. 'Fingerprints' show the COSFIRE filters response to a given feature, where the highest response is depicted in a higher grey level. Similar features in two separate images result in similar 'fingerprints'.

A detailed description of the formulation is beyond of the scope of our work, instead we refer the reader to [46] for details. However, an example is shown below. Fig. 10b shows the fingerprint formed for the vicinity (Fig. 10a) of reference point, q_1 , where the reference point is located in the centre of the search window of the SE image. Tuned operators can detect the same or similar microstructural features regardless of their rotation, scale, reflection and contrast inversion [46]. This can be seen in Fig. 10c, which shows the matching fingerprint to the fingerprint in Fig. 10b located on BC image search patch (Fig. 10d).

Appendix. Moving Least Squares for digital image deformation

Image deformation techniques have been used for animations [74], morphing [46,75–78] and medical imaging [79], where a set of handles (e.g. keypoints, lines, meshes, grids, etc.) are used to control the deformations. The COSFIRE filter locates the distorted positions of these keypoints, p_i (see the previous appendix, entitled 'COSFIRE filters for microstructure pattern recognition'), on the BC image, the image distortion corrections for the given points in the image are corrected by a Moving Least Squares (MLS) method [47,80–82]. MLS is an approximation method of interpolation of irregularly spaced locations or points [83].

The technique requires that the points in the undeformed image

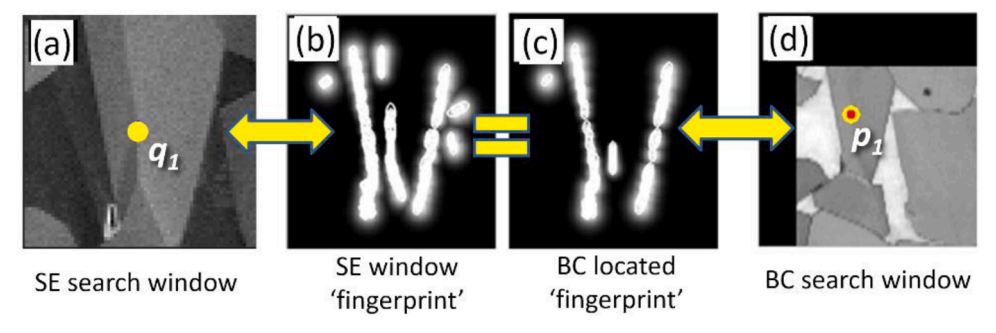
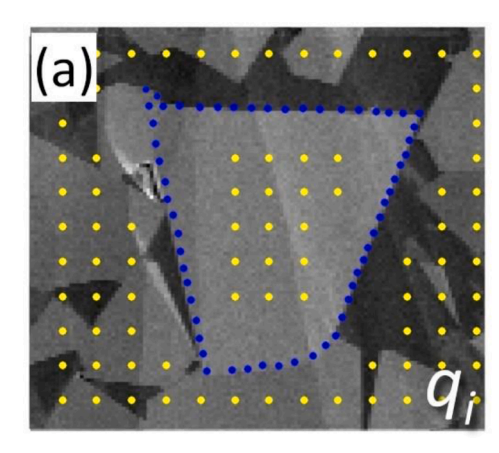


Fig. 10. SE/EBSD image pair matching. (a) SE image patch for the formation of the COSFIRE operator, (b) the 'fingerprint' from the SE patch, (c) the matching 'fingerprint' from the BC image search patch, in (d). Note: The reference point, q_I , and the detected point, p_I , correspond to the centres of the search window of the SE image.



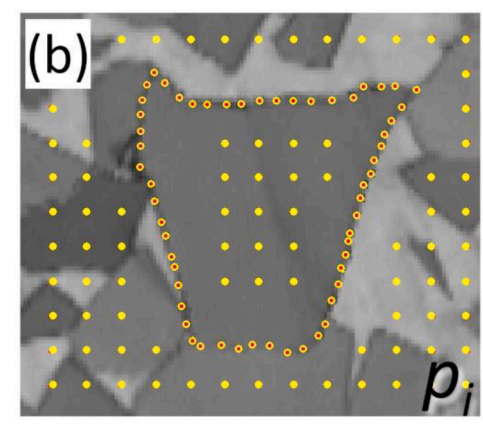


Fig. 11. 'Short-Range Co-registration' applied to the image in Fig. 4:(a) SE image with two sets of reference points, q_{ij} yellow - generated by the software, blue - selected along the grain boundary; (b) BC image with the two sets of 'deformed' points, p_{ij} yellow - generated by the software, orange - selected along the grain boundary.

correspond to the points in the deformed image and must satisfy the following properties [47];

Interpolation: The deformed points should map directly to the undeformed points.

Smoothness: The interpolation should produce a smooth deformation

Identity: If the deformed points are the same as the undeformed points then the interpolation should be the identity function; i.e. copy the point without change.

Rigidity: To produce rigid-as-possible deformations.

This image deformation technique is solved in a small linear system at each point in a uniform grid. This facilitates fast deformation of grids consisting of tens of thousands of points in real time (< 10 ms) [47].

Appendix. Short-range co-registration description

This part of the correction represents a proof of concept, where the process involves a combination of automatic and manual steps. In the section entitled 'The short-range distortion correction procedure' the importance of this correction is demonstrated. Further details of this correction are discussed here.

First, an automatic fine grid of points with an arbitrary spacing (here 10 pixels) is generated in the same location on both SE and BC images pairs (grids of yellow points in Fig. 11). This operation allows pinning the areas of BC image which are correctly co-registered by the LRC. Next, points are manually defined, on the SE image, along features such as the grain boundaries for the local co-registration (blue points in Fig. 11a), and the software automatically removes previously generated points located in the vicinity of selected grain boundaries on both SE and BC images. The reader must be reminded here that the short-range coregistration makes the assumption that the SE image is the correct reference image. The SE image contains a mixture of signals from atomic number, electron channelling (orientation, defect structure) and topography. Therefore any mis-interpretation of the image or incorrect positioning of the points will be retained in the final corrected BC image from the EBSD map. Next, the corresponding points are manually defined on a BC image; red points in Fig. 11b. An automatic MLS image morphing algorithm uses the points to correct the BC images, see Fig. 4 in the section entitled 'The short-range distortion correction procedure' for the results of this method.

References

- G. Nolze, Image distortions in SEM and their influences on EBSD measurements, Ultramicroscopy 107 (2007) 172–183, https://doi.org/10.1016/j. ultramic.2006.07.003.
- [2] S. Maraghechi, J.P.M. Hoefnagels, R.H.J. Peerlings, M.G.D. Geers, Correction of scan line shift artifacts in scanning electron microscopy: an extended digital image correlation framework, Ultramicroscopy (2018) 187, https://doi.org/10.1016/j. ultramic.2018.01.002.
- [3] R. Flatabø, A. Coste, M.M. Greve, A systematic investigation of the charging effect in scanning electron microscopy for metal nanostructures on insulating substrates, J. Microsc. (2017) 265, https://doi.org/10.1111/jmi.12497.
- [4] L.A. Giannuzzi, F.A. Stevie, Introduction to Focused Ion beams: Instrumentation, theory, Techniques and Practice, 2005, https://doi.org/10.1007/b101190.
- [5] B.E. Sorensen, J. Hjelen, H.W. Ånes, T. Breivik, Recent features in EBSD, including new trapezoidal correction for multi-mapping, IOP Conf. Ser. Mater. Sci. Eng. (2020), https://doi.org/10.1088/1757-899X/891/1/012021.
- [6] A.J. Schwartz, M. Kumar, B.L. Adams, D.P. Field, Electron Backscatter Diffraction in Materials Science, 2009. https://doi.org/10.1007/978-0-387-88136-2.
- [7] D. Rowenhorst, Removing Imaging Distortions Through Automatic Stitching of EBSD Mosaics, Microsc. Microanal. (2013) 19, https://doi.org/10.1017/ s1431927613006193.
- [8] A.L. Pilchak, A.R. Shiveley, J.S. Tiley, D.L. Ballard, AnyStitch: a tool for combining electron backscatter diffraction data sets, J. Microsc. (2011) 244, https://doi.org/ 10.1111/j.1365-2818.2011.03496.x.
- [9] A. Winkelmann, G. Nolze, G. Cios, T. Tokarski, P. Bala, Refined calibration model for improving the orientation precision of electron backscatter diffraction maps, Materials (Basel) 13 (2020), https://doi.org/10.3390/ma13122816.
- [10] B. Winiarski, G.S. Schajer, P.J. Withers, Surface Decoration for Improving the Accuracy of Displacement Measurements by Digital Image Correlation in SEM, Exp. Mech. (2012), https://doi.org/10.1007/s11340-011-9568-y.
- [11] B. Winiarski, A. Gholinia, K. Mingard, M. Gee, G.E. Thompson, P.J. Withers, Broad Ion Beam Serial Section Tomography, Ultramicroscopy (2017), https://doi.org/ 10.1016/j.ultramic.2016.10.014.
- [12] F.J. Humphreys, Grain and subgrain characterisation by electron backscatter diffraction, J. Mater. Sci. (2001), https://doi.org/10.1023/A:1017973432592
- [13] T.L. Burnett, P.J. Withers, Completing the picture through correlative characterization, Nat. Mater. (2019), https://doi.org/10.1038/s41563-019-0402-0
- [14] G. Spanos, D.J. Rowenhorst, A.C. Lewis, A.B. Geltmacher, Combining serial sectioning, EBSD analysis, and image-based finite element modeling, MRS Bull (2008), https://doi.org/10.1557/mrs2008.124.
- [15] M.P. Echlin, T.L. Burnett, A.T. Polonsky, T.M. Pollock, P.J. Withers, Serial sectioning in the SEM for three dimensional materials science, Curr. Opin. Solid State Mater. Sci. (2020), 100817, https://doi.org/10.1016/j.cossms.2020.100817.
- [16] A. Gholinia, M. Curd, E. Bousser, K. Taylor, T. Hosman, S. Coyle, M.H. Shearer, J. Hunt, P.J. Withers, Coupled Broad Ion Beam-Scanning Electron Microscopy (BIB-SEM) for polishing and three dimensional (3D) Serial Section Tomography (SST), Ultramicroscopy (2020), 112989, https://doi.org/10.1016/j. ultramic.2020.112989.
- [17] J. Alkemper, P.W. Voorhees, Quantitative serial sectioning analysis, J. Microsc. (2001), https://doi.org/10.1046/j.1365-2818.2001.00832.x.
- [18] J.E. Spowart, H.M. Mullens, B.T. Puchala, Collecting and Analyzing Microstructures in Three Dimensions: a Fully Automated Approach, JOM (2003), https://doi.org/10.1007/s11837-003-0173-0.
- [19] A.C. Lewis, A.B. Geltmacher, Image-based modeling of the response of experimental 3D microstructures to mechanical loading, Scr. Mater. (2006), https://doi.org/10.1016/j.scriptamat.2006.01.043.
- [20] J. Madison, J.E. Spowart, D.J. Rowenhorst, J. Fiedler, T.M. Pollock, Characterization of three-dimensional dendritic structures in nickel-base single

- crystals for investigation of defect formation, Proc. Int. Symp. Superalloys (2008), https://doi.org/10.7449/2008/superalloys 2008 881 888.
- [21] J.P. Hegdal, T.R. Tofteberg, T. Schjelderup, E.L. Hinrichsen, F. Grytten, A. Echtermeyer, Thermal conductivity of anisotropic, inhomogeneous high-density foam calculated from three-dimensional reconstruction of microtome images, J. Appl. Polym. Sci. (2013), https://doi.org/10.1002/app.39238.
- [22] T. Hashimoto, X. Zhou, C. Luo, K. Kawano, G.E. Thompson, A.E. Hughes, P. Skeldon, P.J. Withers, T.J. Marrow, A.H. Sherry, Nanotomography for understanding materials degradation, Scr. Mater. (2010), https://doi.org/ 10.1016/j.scriptamat.2010.06.031.
- [23] G.E. Thompson, T. Hashimoto, X.L. Zhong, M. Curioni, X. Zhou, P. Skeldon, P. J. Withers, J.A. Carr, A.G. Monteith, Revealing the three dimensional internal structure of aluminium alloys, Surf. Interface Anal. (2013), https://doi.org/10.1002/sia.5221.
- [24] M.P. Echlin, A. Mottura, C.J. Torbet, T.M. Pollock, A new TriBeam system for three-dimensional multimodal materials analysis, Rev. Sci. Instrum. 83 (2012), 023701, https://doi.org/10.1063/1.3680111.
- [25] T.L. Burnett, R. Kelley, B. Winiarski, L. Contreras, M. Daly, A. Gholinia, M. G. Burke, P.J. Withers, Large volume serial section tomography by Xe Plasma FIB dual beam microscopy, Ultramicroscopy (2016), https://doi.org/10.1016/j.ultramic.2015.11.001
- [26] G. Desbois, J.L. Urai, F. Pérez-Willard, Z. Radi, S. Offern, I. Burkart, P.A. Kukla, U. Wollenberg, Argon broad ion beam tomography in a cryogenic scanning electron microscope: a novel tool for the investigation of representative microstructures in sedimentary rocks containing pore fluid, J. Microsc. (2013), https://doi.org/10.1111/jmi.12011.
- [27] B. Winiarski, C. Rue, P.J. Withers, Plasma FIB Spin Milling for Large Volume Serial Sectioning Tomography, Microsc. Microanal. (2019), https://doi.org/10.1017/ s1431027610002484
- [28] A. Gholinia, I. Brough, J. Humphreys, D. McDonald, P. Bate, An investigation of dynamic recrystallisation on Cu–Sn bronze using 3D EBSD, Mater. Sci. Technol. 26 (2010) 685–690, https://doi.org/10.1179/026708309X12547309760966.
- [29] A. Gholinia, I. Brough, J. Humphreys, P. Bate, A 3D FIB investigation of dynamic recrystallization in a Cu-Sn bronze, Mater. Sci. Forum (2012), https://doi.org/ 10.4028/www.scientific.net/MSF.715-716.498.
- [30] A. Gholinia, I. Brough, J. Humphreys, D. McDonald, P. Bate, A 3D EBSD Investigation of Dynamic Recrystallisation in a Cu-Sn Bronze, Microsc. Microanal. 15 (2009) 406–407, https://doi.org/10.1017/S1431927609093271.
- [31] A. Bastos, S. Zaefferer, D. Raabe, Three-dimensional EBSD study on the relationship between triple junctions and columnar grains in electrodeposited Co-Ni films, J. Microsc. (2008), https://doi.org/10.1111/j.1365-2818.2008.02008.x.
 [32] I. Borgh, P. Hedström, J. Odqvist, A. Borgenstam, J. Ågren, A. Gholinia,
- [32] I. Borgh, P. Hedström, J. Odqvist, A. Borgenstam, J. Ågren, A. Gholinia, B. Winiarski, P.J. Withers, G.E. Thompson, K. Mingard, M.G. Gee, On the threedimensional structure of WC grains in cemented carbides, Acta Mater (2013), https://doi.org/10.1016/j.actamat.2013.05.008.
- [33] J.C. Stinville, M.P. Echlin, D. Texier, F. Bridier, P. Bocher, T.M. Pollock, Sub-Grain Scale Digital Image Correlation by Electron Microscopy for Polycrystalline Materials during Elastic and Plastic Deformation, Exp. Mech. 56 (2016), https://doi.org/10.1007/s11340-015-0083-4.
- [34] A.D. Kammers, S. Daly, Digital Image Correlation under Scanning Electron Microscopy: methodology and Validation, Exp. Mech. (2013) 53, https://doi.org/ 10.1007/s11340-013-9782-x.
- [35] A.D. Kammers, S. Daly, Self-Assembled Nanoparticle Surface Patterning for Improved Digital Image Correlation in a Scanning Electron Microscope, Exp. Mech. (2013) 53, https://doi.org/10.1007/s11340-013-9734-5.
- [36] Z. Chen, W. Lenthe, J.C. Stinville, M. Echlin, T.M. Pollock, S. Daly, High-Resolution Deformation Mapping Across Large Fields of View Using Scanning Electron Microscopy and Digital Image Correlation, Exp. Mech. (2018) 58, https://doi.org/ 10.1007/s11340-018-0419-y.
- [37] M.A. Charpagne, J.C. Stinville, P.G. Callahan, D. Texier, Z. Chen, P. Villechaise, V. Valle, T.M. Pollock, Automated and quantitative analysis of plastic strain localization via multi-modal data recombination, Mater. Charact. (2020) 163, https://doi.org/10.1016/j.matchar.2020.110245.
- [38] W.C. Lenthe, M.P. Echlin, A. Trenkle, M. Syha, P. Gumbsch, T.M. Pollock, Quantitative voxel-to-voxel comparison of TriBeam and DCT strontium titanate three-dimensional data sets, J. Appl. Crystallogr. (2015) 48, https://doi.org/ 10.1107/S1600576715009231.
- [39] R.R. Keller, R.H. Geiss, Transmission EBSD from 10nm domains in a scanning electron microscope, J. Microsc. (2012) 245, https://doi.org/10.1111/j.1365-2818-2011-03566 x
- [40] P.W. Trimby, Orientation mapping of nanostructured materials using transmission Kikuchi diffraction in the scanning electron microscope, Ultramicroscopy (2012) 120, https://doi.org/10.1016/j.ultramic.2012.06.004.
- [41] A. Garner, A. Gholinia, P. Frankel, M. Gass, I. Maclaren, M. Preuss, The microstructure and microtexture of zirconium oxide films studied by transmission electron backscatter diffraction and automated crystal orientation mapping with transmission electron microscopy, Acta Mater (2014), https://doi.org/10.1016/j. actamat 2014 07 062
- [42] M. Meisnar, A. Vilalta-Clemente, A. Gholinia, M. Moody, A.J. Wilkinson, N. Huin, S. Lozano-Perez, Using transmission Kikuchi diffraction to study intergranular stress corrosion cracking in type 316 stainless steels, Micron (2015), https://doi. org/10.1016/j.micron.2015.04.011.
- [43] P.G. Callahan, M. De Graef, Dynamical electron backscatter diffraction patterns. Part I: pattern simulations, Microsc. Microanal. (2013), https://doi.org/10.1017/ S1431927613001840.

- [44] D. Roşca, A. Morawiec, M. De Graef, A new method of constructing a grid in the space of 3D rotations and its applications to texture analysis, Model. Simul. Mater. Sci. Eng. (2014), https://doi.org/10.1088/0965-0393/22/7/075013.
- [45] V.S. Tong, A.J. Knowles, D. Dye, T.Ben Britton, Rapid electron backscatter diffraction mapping: painting by numbers, Mater. Charact. (2019), https://doi. org/10.1016/j.matchar.2018.11.014.
- [46] G. Azzopardi, N. Azzopardi, Trainable COSFIRE Filters for Keypoint Detection and Pattern Recognition, IEEE Trans. Pattern Anal. Mach. Intell. 35 (2013) 490–503, https://doi.org/10.1109/TPAMI.2012.106.
- [47] S. Schaefer, T. McPhail, J. Warren, Image deformation using moving least squares, ACM Trans. Graph. 25 (2006) 533, https://doi.org/10.1145/1141911.1141920.
- [48] Y. Torres, R. Bermejo, F.J. Gotor, E. Chicardi, L. Llanes, Analysis on the mechanical strength of WC-Co cemented carbides under uniaxial and biaxial bending, Mater. Des. (2014), https://doi.org/10.1016/j.matdes.2013.10.051.
- [49] C. Liu, N. Lin, Y. He, C. Wu, Y. Jiang, The effects of micron WC contents on the microstructure and mechanical properties of ultrafine WC-(micron WC-Co) cemented carbides, J. Alloys Compd. (2014), https://doi.org/10.1016/j. iallcom.2014.01.090.
- [50] K. Mannesson, I. Borgh, A. Borgenstam, J. Ågren, Abnormal grain growth in cemented carbides - Experiments and simulations, Int. J. Refract. Met. Hard Mater. (2011), https://doi.org/10.1016/j.ijrmhm.2011.02.008.
- [51] S.A. McDonald, P. Reischig, C. Holzner, E.M. Lauridsen, P.J. Withers, A.P. Merkle, M. Feser, Non-destructive mapping of grain orientations in 3D by laboratory X-ray microscopy, Sci. Rep. 5 (2015), https://doi.org/10.1038/srep14665.
- [52] A. Trenkle, M. Syha, W. Rheinheimer, P.G. Callahan, L. Nguyen, W. Ludwig, W. Lenthe, M.P. Echlin, T.M. Pollock, D. Weygand, M. Graef, M.J. Hoffmann, P. Gumbsch, Nondestructive evaluation of 3D microstructure evolution in strontium titanate, J. Appl. Crystallogr. (2020) 53, https://doi.org/10.1107/S160057672000093X.
- [53] B. Roebuck, I. Birks-Agnew, C. Phatak, A comparison of the linear intercept and equivalent circle methods for grain size measurement in WC/Co hardmetals, NPL Rep. MATC(A). (2004).
- [54] Oxford Instruments HKL, HKL Channel5 Manual, Denmark, Hobro, 2008.
- [55] W. Skrotzki, Introduction to texture analysis: macrotexture, microtexture and orientation mapping. By Olaf Engler and Valerie Randle. Pp. 456. 2nd ed. Boca Raton: CRC Press, 2010. Price (paperback) USD 129.95. ISBN 978-1-4200-6365-3, J. Appl. Crystallogr. 43 (2010). https://doi.org/10.1107/s0021889810014548.
- [56] S. Giffin, R. Littke, J. Klaver, J.L. Urai, Application of BIB-SEM technology to characterize macropore morphology in coal, Int. J. Coal Geol. (2013), https://doi. org/10.1016/j.coal.2013.02.009.
- [57] I. Markovsky, S. Mahmoodi, Least-Squares Contour Alignment, IEEE Signal Process. Lett. (2009), https://doi.org/10.1109/LSP.2008.2008588.
- [58] K. Mannesson, J. Jeppsson, A. Borgenstam, J. Gren, Carbide grain growth in cemented carbides, Acta Mater (2011), https://doi.org/10.1016/j. actamat.2010.11.056.
- [59] Y.J. Park, N.M. Hwang, D.Y. Yoon, Abnormal growth of faceted (WC) grains in a (Co) liquid matrix, Metall. Mater. Trans. A. 27 (1996) 2809–2819, https://doi.org/ 10.1007/BF02652373.
- [60] M.K. Kang, D.Y. Kim, N.M. Hwang, Ostwald ripening kinetics of angular grains dispersed in a liquid phase by two-dimensional nucleation and abnormal grain growth, J. Eur. Ceram. Soc. (2002), https://doi.org/10.1016/S0955-2219(01) 00370-3.
- [61] G.S. Rohrer, C.L. Rohrer, W.W. Mullins, Coarsening of Faceted Crystals, J. Am. Ceram. Soc. 85 (2002) 675–682, https://doi.org/10.1111/j.1151-2916.2002. tb00149.x.
- [62] A.A. Wahab, M.V. Kral, 3D analysis of creep voids in hydrogen reformer tubes, Mater. Sci. Eng. A. (2005), https://doi.org/10.1016/j.msea.2005.08.223.
- Mater. Sci. Eng. A. (2005), https://doi.org/10.1016/j.msea.2005.08.223.
 [63] A. Trueman, S. Knight, J. Colwell, T. Hashimoto, J. Carr, P. Skeldon, G. Thompson, 3-D tomography by automated in situ block face ultramicrotome imaging using an FEG-SEM to study complex corrosion protective paint coatings, Corros. Sci. (2013), https://doi.org/10.1016/j.corsci.2013.06.021.
- [64] S. Lay, C.H. Allibert, M. Christensen, G. Wahnström, Morphology of WC grains in WC-Co alloys, Mater. Sci. Eng. A. 486 (2008) 253–261, https://doi.org/10.1016/j. msea.2007.09.019.
- [65] F.C. Phillips, An Introduction to Crystallography, 4th ed., LONGMAN, Bugay, Suffolk, U.K., 1971.
- [66] G.S. Rohrer, C.L. Rohrer, W.W. Mullins, Nucleation Energy Barriers for Volume-Conserving Shape Changes of Crystals with Nonequilibrium Morphologies, J. Am. Ceram. Soc. 84 (2001) 2099–2104, https://doi.org/10.1111/j.1151-2916.2001. tb00965.x.
- [67] R.M. German, Coarsening in sintering: grain shape distribution, grain size distribution, and grain growth kinetics in solid-pore systems, Crit. Rev. Solid State Mater. Sci. (2010), https://doi.org/10.1080/10408436.2010.525197.
- [68] K.P. Mingard, B. Roebuck, H.G. Jones, M. Stewart, D. Cox, M.G. Gee, Visualisation and measurement of hardmetal microstructures in 3D, Int. J. Refract. Met. Hard Mater. 71 (2018) 285–291, https://doi.org/10.1016/j.ijrmhm.2017.11.023.
- [69] G. Azzopardi, N. Strisciuglio, M. Vento, N. Petkov, Trainable COSFIRE filters for vessel delineation with application to retinal images, Med. Image Anal. (2015), https://doi.org/10.1016/j.media.2014.08.002.
- [70] S. Marcelja, Mathematical description of the responses of simple cortical cells, J. Opt. Soc. Am. (1980), https://doi.org/10.1364/JOSA.70.001297.
- [71] D. Gabor, Theory of communication. Part 1: the analysis of information, J. Inst. Electr. Eng. - Part III Radio Commun. Eng. 93 (1946) 429–441, https://doi.org/ 10.1049/ii-3-2.1046.0074
- [72] I. Fogel, D. Sagi, Gabor filters as texture discriminator, Biol. Cybern. (1989), https://doi.org/10.1007/BF00204594.

- [73] S.E. Grigorescu, N. Petkov, P. Kruizinga, Comparison of texture features based on Gabor filters, IEEE Trans. Image Process. (2002), https://doi.org/10.1109/ TTP 2002-804262
- [74] D. Vlasic, I. Baran, W. Matusik, J. Popoviç, Articulated mesh animation from multiview silhouettes, ACM Trans. Graph. (2008), https://doi.org/10.1145/ 1360612.1360696.
- [75] S.Y. Lee, K.Y. Chwa, J. Hahn, S.Y. Shin, Image morphing using deformation techniques, J. Vis. Comput. Animat. (1996), https://doi.org/10.1002/(SICI)1099-1778(199601)7:1<3::AID-VIS131>3.0.CO;2-U.
- [76] T.W. Sederberg, S.R. Parry, Free-form deformation of solid geometric models. Comput. Graph. (1986) https://doi.org/10.1145/15886.15903.
- [77] F.L. Bookstein, Principal Warps: thin-Plate Splines and the Decomposition of Deformations, IEEE Trans. Pattern Anal. Mach. Intell. (1989), https://doi.org/ 10.1109/34.24792.
- [78] T. Igarashi, T. Moscovich, J.F. Hughes, As-rigid-as-possible shape manipulation, ACM Trans. Graph. (2005), https://doi.org/10.1145/1073204.1073323.
- [79] K. Penska, L. Folio, R. Bunger, Medical applications of digital image morphing, J. Digit. Imaging. (2007), https://doi.org/10.1007/s10278-006-1050-5.
- [80] G. Backus, F. Gilbert, The Resolving Power of Gross Earth Data, Geophys. J. R. Astron. Soc. (1968), https://doi.org/10.1111/j.1365-246X.1968.tb00216.x.
- [81] L.P. Bos, K. Salkauskas, Moving least-squares are Backus-Gilbert optimal, J. Approx. Theory. (1989), https://doi.org/10.1016/0021-9045(89)90090-7.
- [82] D. Levin, The approximation power of moving least-squares, Math. Comput. 67 (1998) 1517–1532, https://doi.org/10.1090/S0025-5718-98-00974-0.
- [83] D. Shepard, A two-dimensional interpolation function for irregularly-spaced data, in: Proc. 1968 23rd ACM Natl, Conf. -, ACM Press, New York, New York, USA, 1968, pp. 517–524, https://doi.org/10.1145/800186.810616.